In Vivo Biodistribution of Amino-Functionalized Ceria Nanoparticles in Rats Using Positron Emission Tomography

ARTICLE *in* MOLECULAR PHARMACEUTICS · NOVEMBER 2012

Impact Factor: 4.38 · DOI: 10.1021/mp300382n · Source: PubMed

molecular pharmaceutics

Article

pubs.acs.org/molecularpharmaceutics

In Vivo Biodistribution of Amino-Functionalized Ceria Nanoparticles in Rats Using Positron Emission Tomography

Santiago Rojas,[†,#] Juan Domingo Gispert,[‡,#] Sergio Abad,[†] Mireia Buaki-Sogo,[§] Victor M. Victor,[⊥,∥] Hermenegildo Garcia,*[,§] and Jose Raúl Herance*[,†]

[†]CRC-Centre d'Imatge Molecular (CRC-CIM), Parc de Recerca Biomèdica de Barcelona (PRBB), c/Dr. Aiguader 88, 08003 Barcelona, Spain

[‡]Institut d'Alta Tecnologia, Parc de Recerca Biomèdica de Barcelona (IAT-PRBB), c/Dr. Aiguader 88, 08003 Barcelona, Spain

[§]Departamento de Química and Instituto Universitario de Tecnología Química CSIC-UPV, Universidad Politécnica de Valencia, 46022 Valencia, Spain

[⊥]Fundacion para la Investigacion Sanitaria y Biomedica de la Comunidad Valenciana FISABIO/University Hospital Doctor Peset, Endocrinology Service, Avda Gaspar Aguilar 90, 46017 Valencia, Spain

[∥]Department of Physiology, Pharmacology and CIBER CB06/04/0071 Research Group, CIBER Hepatic and Digestive Diseases, University of Valencia, Spain

Supporting Information

ABSTRACT: A variety of nanoparticles have been proposed for several biomedical applications. To gauge the therapeutic potential of these nanoparticles, in vivo biodistribution is essential and mandatory. In the present study, ceria nanoparticles (5 nm average particle size) were labeled with ^{18}F to study their in vivo biodistribution in rats by positron emission tomography (PET). The ^{18}F isotope was anchored by reaction of *N*-succinimidyl 4-[^{18}F]fluorobenzoate (^{18}F-SFB) with a modified nanoparticle surface obtained by silylation with 3-aminopropylsilyl. Radiolabeled ceria nanoparticles accumulated mainly in lungs, spleen, and liver. Metabolic products of the radiolabeled nanoparticulate material were excreted into the urinary tract.

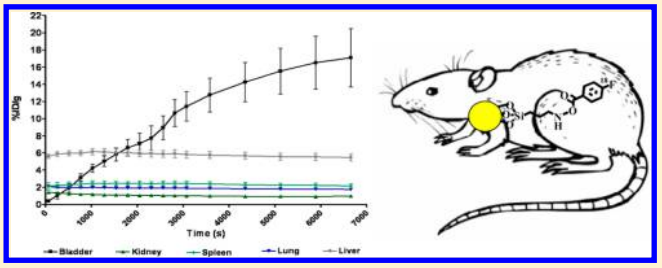

KEYWORDS: *ceria nanoparticles, PET, pharmacokinetics, in vivo evaluation, rodent*

INTRODUCTION

During the past decade, applications of nanoparticles have attracted increasing interest in different fields, such as material science, chemistry, biology, and therapeutics.[1−6] The interest in nanoparticle applications arises from its capacity to load and release molecules and from the high percentage of external atoms and surface area of nanoparticulate materials that allow, among other possibilities, covalent anchoring of several functional components on their surface. Moreover, the physicochemical composition of nanoparticles can be engineered to make them inert or reactive versus a reactant or the environment. Particularly in biology and biomedicine, nanoparticles have been proposed for different uses, such as drug delivery systems or imaging agents, among others.[7−9] Prerequisites for their use in biomedical applications are good biocompatibility, sufficient blood residence time to reach the target, efficient clearance from the body, and high accumulation in the target organs to be efficient while minimizing side effects. In consequence, in vivo pharmacokinetic characterization of nanoparticles in animal models is fundamental before considering their use in humans.

Evaluation of in vivo or ex vivo biodistibution of nanoparticles can be addressed with different approaches. Noninvasive radioactive molecular imaging techniques, such as single-photon emission computed tomography (SPECT) and positron emission tomography (PET) enable the absolute quantification of pharmacokinetics in preclinical and human subjects.[10−16] Application of these methods for imaging nanoparticle biodistribution provides sensitive and quantitatively accurate in vivo measurements that can serve as a basis to explore their utility as therapeutic or diagnostic agents.

Ceria nanoparticles (CeNPs) contain a high density of oxygen vacancies in their structure thanks to the presence of Ce ions in the 3+ oxidation state.[17,18] These structural defects explain the size[19,20] and the behavior of CeNPs as a *n*-type semiconductor,[21−24] as well as the exceptional performance of this material in catalytic processes that involve oxygen activation, such as oxidation of CO to CO_2.[25−28] In addition,

Received: July 12, 2012
Revised: October 11, 2012
Accepted: November 9, 2012
Published: November 9, 2012

these oxygen vacancies are responsible for the ability of CeNPs to store oxygen during the lean phase and to give oxygen back to metal particles during the oxygen-rich phase. This phenomenon is known as oxygen storage capacity of ceria.[29−31] Deposition of metal nanoparticles on ceria surface or the presence of impurities may drastically increase the density of oxygen vacancies present in ceria, thus enhancing its catalytic activity.[32,33] Furthermore, ceria presents versatile acid−base properties, depending on the composition or temperature of the pretreatment.[34,35] A reductive pretreatment of ceria increases its basicity. These acid−base and redox properties allow ceria to catalyze different organic reactions, such as dehydration of alcohols and ketonization by their acid−base sites; reduction and oxidation of organic compounds by the redox centers, and addition, substitution, isomerization, or ring-opening reaction by a mixture of acid−base and redox sites.[36]

The redox properties of CeNPs have raised interest in biomedicine, and these nanoparticles have been postulated for some therapeutic applications.[37−42] Most of the potential uses of CeNPs are mainly based on the reduction of the concentration of radical species in tissues given its antioxidant capacity. CeNPs have been tested in vitro and in vivo as quenchers of reactive oxygen species in some kinds of cells and as a radiation protector, cardioprotector, or endothelial inflammation reducer.[43−47]

To precisely gauge the potential of CeNPs in biomedicine, it is necessary to evaluate their biodistribution. To our knowledge, only a few studies have determined the pharmacokinetic properties of CeNPs in rodents. The aim of these previous reports was to explore the safety hazards of exposure to CeNPs rather than evaluation of their biomedical potential. For this reason, some studies considered the pulmonary and oral absorption of CeNPs as these routes are the most common ways of inadvertent exposure due to environmental contamination.[48−50] In another four papers, the material was administered intravenously to evaluate its ability to cross the blood brain barrier and the blood clearance capacity.[51−54] Finally, the pharmacokinetics of CeNPs during a period ranging from 1 to 90 days[55] as well as their in vivo biodistribution and antioxidant capacity after intravenous and intraperitoneal administration was explored.[56] However, these previous studies did not report biodistribution data in the initial minutes after ceria administration, which is fundamental to precisely evaluate the pharmacokinetics upon a single administration.

In this work, we present the biodistribution in rodents of CeNPs functionalized with amino groups in which a 4-[^{18}F]fluorobenzoyl moiety has been anchored to obtain pharmacokinetic data by PET. This methodology enables the in vivo quantification of the labeled compound in each organ, especially during the initial minutes after administration when vascular trapping and phagocytosis occurs.

EXPERIMENTAL SECTION

Materials and Instrumentation. All the reactants for synthesis were purchased from Advanced Biochemical Compounds (ABX), Sigma-Aldrich, and Scharlab. QMA, C18 HELA cartridges were obtained from Waters. The size of the nanoparticles was determined by transmission electron microscopy (TEM) using a Philips CM300 FEG system with an operating voltage of 100 kV by counting a statistically relevant number of particles. TEM samples were prepared by placing microdrops of ceria colloidal solutions directly onto a copper grid coated with a carbon film (200 mesh). Powder XRD patterns were recorded with a Philips X'Pert diffractometer using the Cu Kα radiation at a scan rate of 2° min^{-1}. FT-IR spectra were recorded on a Nicolet 710 FT-IR spectrophotometer using self-supported wafers of ceria compressed to 2 Ton cm^{-2} for 2 min. The cyclotron used for ^{18}F production was an 18/9 model from IBA. Radiosynthesis was done with different assembled Eckert & Ziegler modules. Analytical and purification analyses were performed by HPLC using an Agilent 1100 series apparatus coupled to a diode array UV−vis Agilent 100 detector and a Raytest GINA isotopic detector. The centrifuge apparatus used was a Hettich-Zentrifugen.

Formation of CeNPs. CeNPs were prepared by hydrolysis of $Ce(NO_3)_3$ at pH = 9 using $(NH_4)OH$ as previously reported.[57] Small CeNPs were obtained under controlled pH conditions from cerium nitrate. Briefly, an ammonia aqueous solution (1.12 L, 0.8 M) was added under stirring and at ambient temperature over 375 mL of a $Ce(NO_3)_3$ (0.8 M). The colloidal dispersion of CeNPs was heated in a poly(ethylene terephthalate) vessel at 100 °C over 24 h. The resulting yellow precipitate was filtered and dried under vacuum overnight. The cerium oxide synthesized has, owing to the small size of the nanoparticles, a very high surface area (180 m^2 g^{-1}), measured by isothermal N_2 adsorption at −198 °C using a Micromeritics ASAP2000 and applying the Brunaer−Emmett−Teller algorithm. TEM images were obtained in a Philips microscope operating at 100 kV. A drop of CeNP suspended in water was cast onto a carbon-coated copper grid. Particle size distribution was estimated from the TEM images by averaging the diameter of 150 particles.

Formation of μ-Aminopropyl-Functionalized CeNPs (NH_2−CeNPs). To attach an ^{18}F- radioactive synthon on the surface by using *N*-succinimidyl 4-[^{18}F]fluorobenzoate (^{18}F-SFB), CeNPs were modified by anchoring covalently 3-(aminopropyl)triethoxysilane. Silylation was carried out by stirring at reflux temperature a suspension of 1 g of dehydrated CeO_2 sample (100 °C for 3 h under atmospheric pressure) in toluene containing 0.5 mL of 3-(aminopropyl)triethoxysilane for 2 h. After this time, the mixture was allowed to cool at room temperature, and the 3-(aminopropyl)silyl functionalized ceria was decanted, washed with fresh toluene aliquots (3 × 2 mL), and dried at ambient temperature. The density of aminopropyl groups was determined by thermogravimetry using a Netsch thermobalance under air in the temperature range from ambient to 800 °C and by combustion elemental analysis using a Fisons CHNS analyzer.

Determination of ζ-Potential of CeNPs and NH_2−CeNPs. Water solutions (10 ppm) of CeNPs and NH_2−CeNPs samples were subjected to dynamic light scattering for ζ-potential measurement that was performed in a Zetasizer Malvern Nano Series 2S Instrument.

Catalytic Decomposition of Hydrogen Peroxide. A 100 mL portion of an aqueous H_2O_2 solution having a concentration of 200 ppm was prepared using Milli-Q water and commercial H_2O_2 (30 v/v %, Foret) and placed in an Erlenmeyer flask, then 100 mg of CeNPs was added. The suspension was stirred by applying polychromatic UV light at room temperature. The time conversion was determined by analyzing aliquots (2 mL, filtered through 0.2 μm Nylon filter) that were diluted 10-fold and titrated colorimetrically using $K_2(TiO)(C_2O_4)_2$ in H_2SO_4/HNO_3 monitoring at 420 nm. This

experiment was performed again for NH_2-CeNPs under the same conditions.

Production of ^{18}F-SFB. The synthesis was performed in assembled Eckert & Ziegler modules following the methodology described by Mäding, et al.[58] Briefly, $^{18}F^-$ was produced by bombardment of [^{18}O]-H_2O with protons at 18 MeV energy in the cyclotron. The $^{18}F^-$ was sent then to an automatic module, where it was trapped in a QMA cartridge. It was then extracted toward the reactor by transferring a mixture of 2 mg of K_2CO_3 and 1.8 mg of Kryptofix 222 in 1 mL of a mixture of H_2O/CH_3CN 1:1 through the QMA cartridge. The reactor was then heated at 100 °C and, to dry the $^{18}F^-$ present in the reactor, He flow and vacuum were applied for 5 min. To ensure that the drying process was done correctly, an extra 1 mL of anhydrous CH_3CN was added, drying the mixture as previously. The next step consisted of adding a solution of 5 mg of 4-(*tert*-butoxycarbonylmethyl)phenyl trimethylammonium trifluoromethanesulfonate in 1 mL of anhydrous CH_3CN. The mixture was stirred for 10 min at 90 °C, and then 0.5 mL of 1 M HCl was added. The reaction mixture was heated at 100 °C for 5 min. After cooling to 25 °C, the reaction mixture was diluted with 9 mL of water and passed through a C18 HELA cartridge for solid extraction. Subsequently, 3 mL of CH_3CN was passed through the mentioned cartridge, and the solution was sent to a second reactor. This eluate was treated with 20 μL of 25% methanolic Me_4NOH in 500 μL of CH_3CN, then the reaction mixture was dried at 90 °C, passing a continuous He flow and applying vacuum. Drying was completed by the addition of 3 mL of anhydrous CH_3CN, then a solution of 15 mg of *N*,*N*,*N*′,*N*′-tetramethyl-*O*-(*N*-succinimidyl)uronium tetrafluoroborate in 500 μL of anhydrous CH_3CN was added, and the mixture was heated at 90 °C for 2 min. The mixture was cooled to 25 °C and diluted with 5% aqueous acetic acid. The reaction crude was then purified in a semipreparative HPLC using a Teknokroma Mediterranean Sea-18 (25 × 1 cm, 5 μm) column and working in isocratic mode with a mobile phase composed of CH_3CN/ammonium formate (3.15 g/L of H_2O, pH = 5) 42.5:57.5 at a flow rate of 5 mL/min and monitored by gamma and UV−vis (254 nm) detectors. The desired fraction (9−11 min) was collected over 20 mL of 0.9% saline solution. This solution was passed through a C18 cartridge, rinsed with 20 mL of water, and extracted with 3 mL of anhydrous acetone. The solvent was dried by bubbling N_2, the residue was solved in 200 μL of DMSO, and an aliquot was submitted to quality testing. Quality control was done by HPLC using a Teknokroma Mediterranean Sea-18 (25 × 0.46 cm, 5 μm) column and working at 2 mL/min in gradient mode using CH_3CN/ammonium formate (3.15 g/1 L H_2O pH = 5) as the mobile phase starting with a mixture 10:90 and achieving 40:60 in 10 min. The detection was monitored by gamma and UV−vis (254 nm) detectors obtaining ^{18}F-SFB at 10.3 min. The identity of ^{18}F-SFB was confirmed by coelution with the ^{19}F-standard (SFB), so ^{18}F-SFB was obtained with a yield of 37 ± 5% and with chemical and radiochemical purity exceeding 98% and 102 ± 7 GBq/μmol of specific activity.

Formation of ^{18}F-Labeled CeNPs (^{18}F-CeNPs). A 2.0 ± 0.3 mg portion of NH_2-CeNPs was stirred at room temperature for 1 h with a solution composed of ∼70 mCi of pure ^{18}F-SFB in a mixture of 150 μL of DMSO and 100 μL of phosphate buffer at pH= 7.4. After this time, 1.8 mL of phosphate buffer at pH = 7.4, was added and the mixture was centrifuged at 4000 rpm for 10 min. The resultant solid was washed twice by centrifugation at 4000 rpm using 2 mL of phosphate buffer. After checking the absence of radioactivity in the supernatant of the centrifuged mixture, the washed ^{18}F-CeNPs solid was dispersed in 2 mL of phosphate buffer, pH = 7.4, +5% Tween 80 and sonicated for 5 min just before injection. Using the described procedure, a radiochemical yield of 17.7 ± 3.0% was obtained after washing.

Animals. Adult male Sprague−Dawley rats weighting 309 ± 8 g (mean ± standard deviation; Charles River, France; n = 5) were used. Animals were housed under controlled laboratory conditions with the temperature maintained at 21 ± 1 °C and humidity at 55 ± 10%. Food and water were available ad libitum. Animal procedures were conducted in strict accordance with the guidelines of the European Communities Directive 86/609/EEC regulating animal research and were approved by the local ethical committee (CEEA-PRBB).

PET Image Acquisition. Animals were anesthetized with isoflurane and received an intravenous bolus injection of the ^{18}F-CeNPs. Doses administered were 4.8 ± 3.1 MBq resuspended in 0.5 mL of saline, and the injection route was the lateral tail veins. Immediately after injection animals were placed in an animal dedicated camera (microPET R4; Concorde, Siemens, Knoxville, TN) for dynamic whole body image acquisition. Whole body data were acquired for 120 min. During the entire acquisition procedure, anesthesia was maintained with a facial mask and a concentration of 2.5% of isoflurane vaporized in O_2.

Image analysis. To obtain the dynamic whole body images (18 frames × 6.7 min/frame), PET data were corrected for nonuniformity, random coincidences, and radionuclide decay and reconstructed with a filtered backprojection algorithm into a matrix size of 128 × 128, a voxel size of 0.85 × 0.85 mm, a slice thickness of 1.21 mm, and an axial field of view covering the full length of the animal (approximately 20 cm). After reconstruction, volumes of interest were manually drawn from the different organs; individual time activity curves were obtained; and finally, the mean time−activity curves were calculated. Activity concentration at the end of the acquisition was used to determine the percentage of injected dose for each gram of tissue (% Id/g).

Ex-Vivo Study. At the end of acquisition, animals were sacrificed, and the different organs were dissected, weighted, and measured in a gamma ray counter (Wallac 1470 Wizard, Perkin-Elmer, Waltham, MA) for ^{18}F radioactivity determination. Radioactivity measured was corrected for decay, injected dose, mass of the tissue sample and animal weight to obtain the percentage of injected dose for each gram of tissue (% Id/g) and the SUVs, respectively

RESULTS

Preparation of ^{18}F-CeNPs. CeNPs were obtained by hydrolysis of Ce^{4+} nitrate salt in water at controlled basic pH and purified by dialysis as indicated in the Experimental section. The average particle size was determined from the width of the XRD peaks and by applying the Scherrer equation, giving an average of 5.6 nm (see Figure 1). The small shifts in the 2θ values of the diffraction peaks after functionalization could reflect the influence of the aminopropylsilyl group surface on ceria nanocrystal high-resolution TEM images that reveals the morphology and shape of the CeNPs (see Figure 2).

Covalent functionalization of the ceria surface with amino groups was carried out by silylation of the surface OH groups in dry organic solvents. This methodology has served in the past to introduce amino groups anchored on the ceria surface.[59]

dx.doi.org/10.1021/mp300382n | *Mol. Pharmaceutics* 2012, 9, 3543−3550

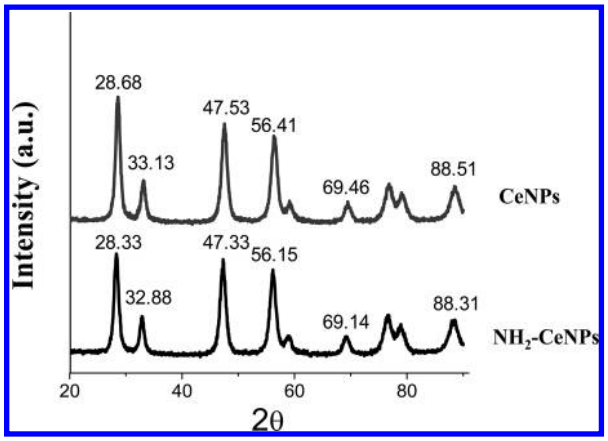

Figure 1. XRD patterns of NH_2−CeNPs and CeNPs.

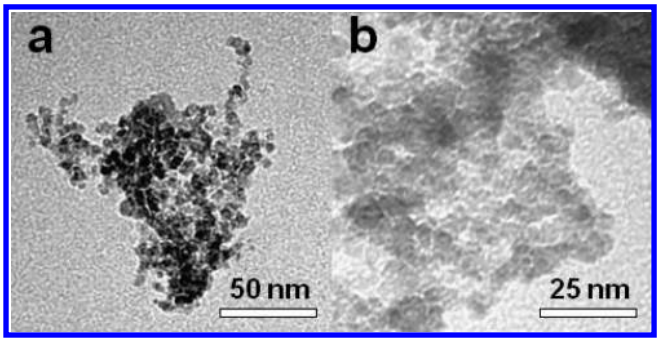

Figure 2. Representative TEM images of CeNPs recorded at two different magnifications, as indicated in the scale bar.

These amino groups will act as tethers and will connect with the isotopically labeled 4-(^{18}F)fluorobenzoyl that will serve to trace the biodistribution of ^{18}F-CeNPs. Scheme 1 illustrates the synthetic route followed to obtain suitable ^{18}F-CeNPs.

Elemental analysis (C and N) indicates that the density of aminopropyl groups is about 4.4 mmol g^{-1}. This loading is also confirmed by thermogravimetry that shows ∼4.2 wt % of organic matter, as evidenced by the weight loss of the sample in the temperature range from 150 to 550 °C (see the Supporting Information).

The presence of 3-aminopropyl groups anchored on the ceria surface is evidenced in the IR spectra of the samples. For aminopropyl groups, the two vibration bands characteristic of symmetric and asymmetric NH_2 and CH_2 stretching at 3270, 3230, 2990, and 2950 cm^{-1} were observed, although their intensity was small because of the low weight percentage of these groups (see Figure 3). The increase in the IR peak width for NH_2−CeNPs compared to CeNPs could be due to an increase in the inhomogeneity of functional groups in the sample.

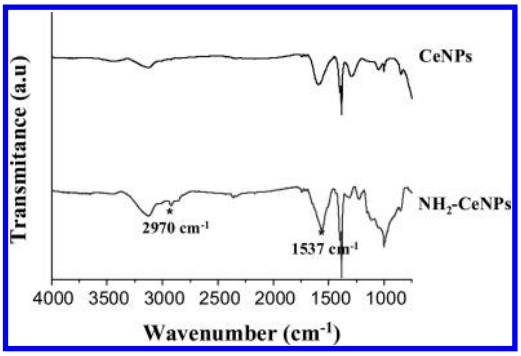

Figure 3. FT-IR spectra of CeNPs (a) and NH_2−CeNPs (b).

It has been proved that ceria nanoparticles can be internalized in cells and exhibit antioxidant activity.[38] It is of interest to provide some information about how surface functionalization with aminopropyl groups modifies the surface and catalytic properties of ceria nanoparticles. To provide some data about this issue, we measured the ζ-potential of CeNPs and NH_2-CeNPs. It was found that the negative CeNP ζ-potential value of −23.5 mV changed to a positive value of 18.5 mV, reflecting the presence of amino groups that will be partly protonated in water at neutral pHs.

Surface functionalization with amino groups is also reflected in a decrease in the catalytic activity of the parent CeNPs for hydrogen peroxide decomposition. Activity as antioxidizing agents is related to their activity to decompose peroxides during aerobic oxidation metabolism. Therefore, H_2O_2 decomposition at neutral pH in water upon illumination can be taken as a model reaction for this process. Figure 4 shows the temporal

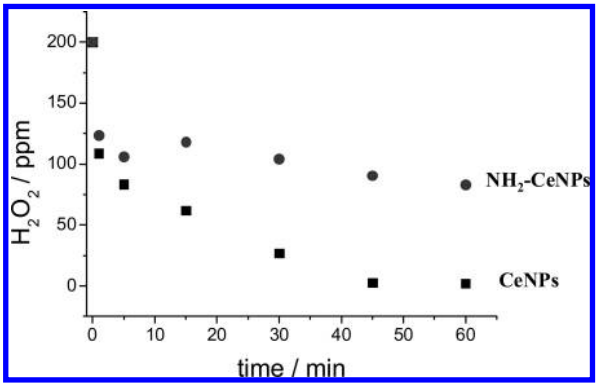

Figure 4. Temporal profile of H_2O_2 concentration in the presence of CeNPs or NH_2-CeNPs. Reaction conditions: initial H_2O_2 concentration, 200 ppm; amount of solid catalyst, 1 g/L; irradiation with polychromatic UV light at room temperature.

profile of H_2O_2 decomposition in the presence of CeNPs and NH_2−CeNPs. As can be seen there, although surface functionalization decreases, the antioxidant activity inherent

Scheme 1. Preparation of ^{18}F-CeNPs from CeNPs for Biodistribution Study in Rodents

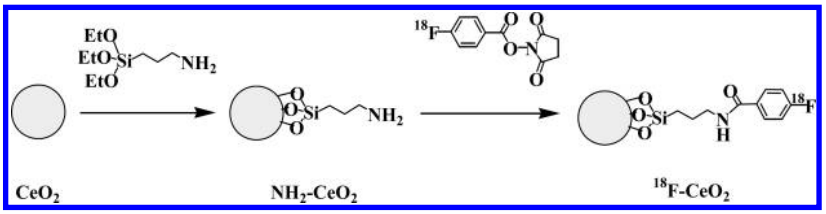

dx.doi.org/10.1021/mp300382n | Mol. Pharmaceutics 2012, 9, 3543−3550

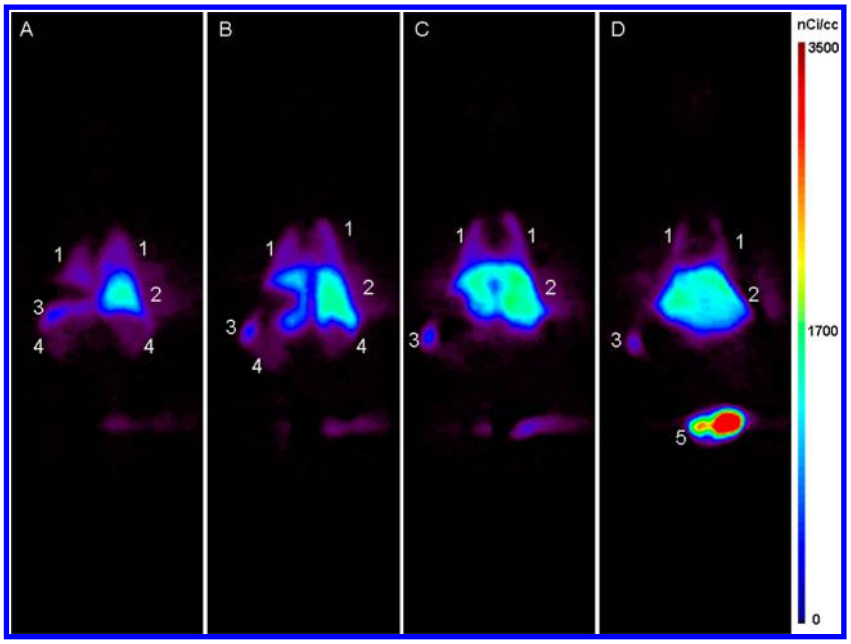

Figure 5. Coronal sections of PET images obtained over 120 min after injection. Organs that presented elevated uptake of the radiolabeled ^{18}F-CeNPs were lungs (1), liver (2), spleen (3), kidneys (4), and bladder (5). Images were obtained 30 (A), 60 (B), 90 (C), and 120 (D) min after ^{18}F-CeNPs administration.

to CeNPs, the functionalized NH_2-CeNPs still have remarkable activity. This diminution in the catalytic activity can be rationalized assuming that a fraction of the surface hydroxyl group acting as active sites in H_2O_2 decomposition have disappeared in the silylation reaction.

In Vivo Pharmacokinetics. Visual inspection of the images showed accumulation of the ^{18}F-CeNPs mainly in the lungs, liver, kidneys, and spleen. The bladder was also clearly visible, especially in the later frames of the dynamic images (see Figure 5).

Time–activity curves obtained from the PET data showed that the activity was almost constant during the whole acquisition period in all the organs, with the exception of the bladder. In fact, in this case, the radioactivity concentration increased along the time of study, reflecting the urinary excretion of the radiolabel (see Figure 6).

Biodistribution at the end of the PET acquisition indicated that the organ exhibiting the highest concentration of radioactivity was the bladder, followed by liver, lungs, spleen, and finally, the kidneys (see Figure 7A). No other organs presented significant accumulations of the ^{18}F-CeNPs.

Ex Vivo Study. Results of the ex vivo study confirmed the organ biodistribution determined from PET images (see Figure 7B). The highest concentration of the radioactivity was observed in bladder followed by liver, spleen, lungs, and kidneys. Additionally, very low levels of radioactivity were present in the intestine and blood. The lowest radioactive concentration of the evaluated organs was found in the brain, with a slightly lower concentration than blood (see Figure 7 B).

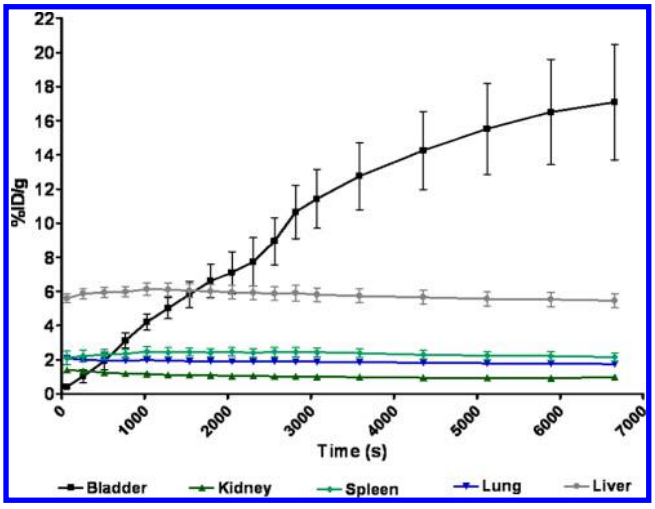

Figure 6. Mean time activity curves of the different organs obtained from PET images after administration of ^{18}F-CeNPs. Bar represents standard deviation.

DISCUSSION

The pharmacokinetic properties of a compound can completely compromise its potential biomedical application. Actually, nanoparticles exhibiting unfavorable biodistribution will be completely useless regardless their in vitro efficacy. Because of the interest evoked in biomedicine for the use of CeNPs as antioxidants, their biodistribution in rats was studied in this work.

After preparation and purification from soluble salts by dialysis, the ceria sample can be functionalized with amino groups by silylation of the surface OH groups. Triethoxysilanes are suitable reagents for surface functionalization under mild conditions in nonaqueous media.[60] The success of the functionalization and the loading of amino groups can be determined by combustion C and N chemical analysis, thermogravimetry, and IR spectroscopy (see Figure 3). Comparison of the thermogravimetric profiles before and after silylation shows differences that are due to the decomposition of the 3-aminopropyl groups introduced in the silylation. The presence of the amino groups and methylene chains can be clearly seen in the FT-IR spectra of the ceria sample after silylation, which shows the expected bands that,

dx.doi.org/10.1021/mp300382n | Mol. Pharmaceutics 2012, 9, 3543–3550

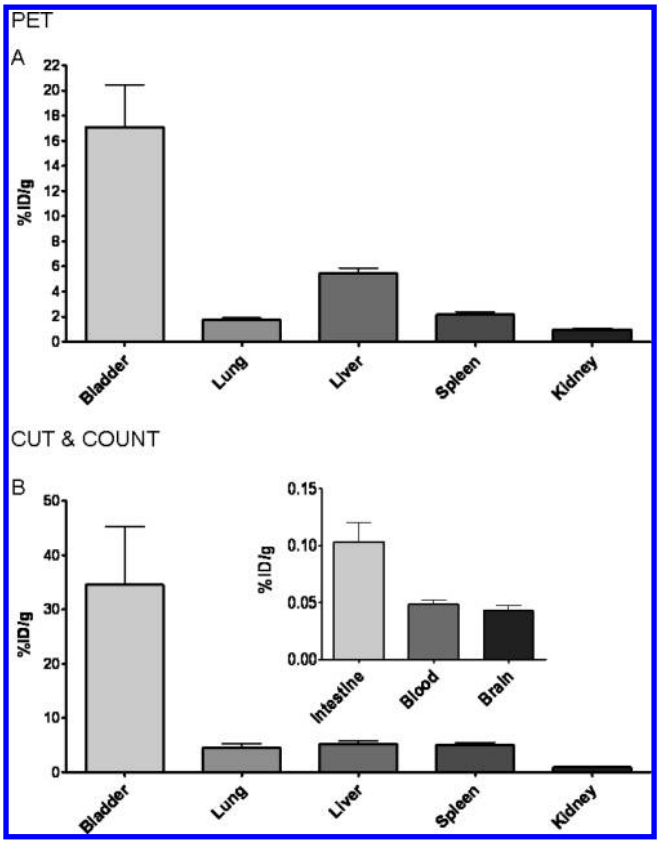

Figure 7. ^{18}F-CeNPs biodistribution results obtained from the PET study (A) and cut and count after 2 h (B). Note the similar radioactive concentration between blood and brain.

obviously, were not present in the original ceria sample and that are compatible with the organic groups.[61] It should be noted, however, that this surface functionalization produces some unavoidable influence on the properties of CeNPs, as evidenced by the change in the ζ-potential and the decrease in the catalytic activity for hydrogen peroxide decomposition.

The purpose of the preparation of these modified CeNPs was to introduce covalently anchored radioactive ^{18}F atoms, by reaction of the surface CeNPs amino groups with ^{18}F-SFB. This labeling strategy enables tracking the distribution of these nanoparticles in the organs of living rodents by PET and, ex vivo, by measuring the radioactivity in each organ.

Our results indicate that as soon as the ^{18}F-CeNPs entered into the blood, they became trapped in organs such as the lungs, liver, and spleen. In fact, time-activity curves showed that the concentration observed in these organs for the initial frames of the study remained almost constant until the end of the imaging study. The uptake of ^{18}F-CeNPs in the lungs strongly suggests trapping in the pulmonary capillary by size exclusion. In contrast, the accumulation observed in the liver and spleen could potentially reflect phagocytosis of ^{18}F-CeNPs by the reticuloendothelial system. This system is known to phagocyte foreign materials of sizes similar to the administered ceria nanoparticles,[12] and depending on the particle characteristics, is one of the major causes of nanoparticle removal from blood. Usually, the concentration of a compound that is reversibly trapped in the organs should decrease proportionally to its excretion rate. In our case, the ^{18}F-CeNPs concentration in the liver, lungs, and spleen remained constant despite the observed progressive excretion. This behavior is compatible with the irreversible trapping of the nanomaterial into macrophages or, in the case of the lungs, in its vascular network. This accumulation in organs of the reticuloendothelial system and in the lungs is completely compatible with previous works that evaluated the biodistribution of intravenously administered CeNPs.[51−56] Moreover, the low radioactivity content observed in the intestine indicated that despite the accumulation observed in the liver, the ^{18}F-CeNPs were not excreted through the biliary tract.

The progressive increase in the urinary system could indicate that the fraction of ^{18}F-CeNPs that was not phagocytized and circulates in the bloodstream is excreted through the kidney into urine. Alternatively, the nanoparticles could be metabolized in the organs that trapped them initially, and the resulting metabolites could be excreted into the bloodstream up to urine. The experiments performed to explore these two scenarios indicated that ^{18}F-CeNPs were progressively metabolized in plasma, and the radioactive content found in urine corresponded to soluble metabolites of ^{18}F-CeNPs and not to the intact nanoparticle (see Supporting Information). Similar behavior was reported by other nanoparticles when they were administered intravenously.[10,12]

Results of the ex vivo study confirmed the results obtained in vivo in all the organs evaluated and indicated that after 2 h, almost all the ^{18}F-CeNPs were cleared from the blood. The brain presented the lowest radioactivity content among the evaluated organs. However, the cerebral radiolabel concentration was similar to that of blood. Taking into consideration that the blood pool represents less than 10% of the brain weight, in the event of the total absence of the blood−brain barrier crossing, the expected brain ^{18}F-CeNPs concentration would be one-tenth that of blood. The obtained results strongly suggest that limited amounts of ^{18}F-CeNPs enter the brain or, alternatively, that they remain trapped in the vascular endothelium of the brain. However, no peripheral vascular accumulation was evident from the PET images, thus suggesting that some ^{18}F-CeNPs could enter the brain.

One limitation of the PET studies is that the short half-life of the PET radioisotopes (109 min for ^{18}F) allows for studying only early pharmacokinetics during the first hours post administration. The present study evaluated the biodistribution of ^{18}F-CeNPs up to 2 h after the injection. However, after the initial accumulation in the early minutes, the radioactive concentration remained almost constant, suggesting that ^{18}F-CeNPs could remain in these organs for a much longer time.

In conclusion, ^{18}F-CeNPs were properly obtained by reacting ^{18}F-SFB on the ω-aminopropyl-functionalized CeNPs surface. The biodistribution study in rats showed that the labeled nanoparticles were retained mainly in the lungs and reticuloendothelial system, probably by size exclusion and phagocytosis, respectively. The metabolic products of the ^{18}F-CeNPs were finally excreted into urine. Although the lowest concentration of radiolabel occurred in the brain, it was higher than expected in the event of total impermeability of the blood−brain barrier with respect to the ^{18}F-CeNPs. In this way, the signal observed in this organ was similar to that found in blood, suggesting some penetration of radiolabeled nanoparticles across the blood−brain barrier. Our study shows that PET biodistribution studies are extremely useful and informative for future evaluations of nanoparticles as therapeutic agents.

■ ASSOCIATED CONTENT

Supporting Information

The methodologies followed to determine the nature of the radioactivity in urine and the stability of ^{18}F-CeNPs in plasma. In addition, figures to show the data of the temporal profile for the metabolization of ^{18}F-CeNPs in plasma and the thermogravimetric profile and chemical analysis of the NH_2−CeNPs. This material is available free of change via the Internet at http://pubs.acs.org.

■ AUTHOR INFORMATION

Corresponding Author

*(J.R.H.) Address: CRC-Centre d'Imatge Molecular, c/Dr. Aiguader, 88, Edifici PRBB, 08003 Barcelona, Spain. Phone: +34 93 551 16 00. Fax: +34 93 551 16 01. E-mail: rherance@crccorp.es. (H.G.) Address: Instituto de Tecnología Química CSIC-UPV and Departamento de Química, Universidad Politécnica de Valencia, Av. De los Naranjos s/n, 46022 Valencia, Spain. Phone: +34963877809. Fax: (+34) 963-877-809. E-mail: hgarcia@qim.upv.es.

Author Contributions

#These authors have equally contributed to this work.

Notes

The authors declare no competing financial interest.

■ ACKNOWLEDGMENTS

The present work was supported by the Spanish MICINN (Grants CTQ-2009-11586, CTQ2006-06785, and CTQ2007-67805-AR07, PI10/1195, AP192/11); the Fondo de Investigación Sanitaria (FIS) of the Instituto de Salud Carlos III (Grants PS09/02620, PI10/1195, and PS09/02217), the Generalitat Valenciana (Grant ACOMP/2012/045), La Marató Fundation (Grant 090530), and by CDTI under the CENIT Programme (AMIT Project) and the Spanish Ministry of Science and Innovation. V.M.V. is a recipient of a contract from the Regional Ministry of Health of the Valencian Regional Government and Carlos III Health Institute (CES10/030).

■ REFERENCES

(1) Kim, B. Y.; Rutka, J. T.; Chan, W. C. Nanomedicine. *N. Engl. J. Med.* **2010**, *363*, 2434−2443.

(2) Wang, J.; Byrne, J. D.; Napier, M. E.; DeSimone, J. M. More Effective Nanomedicines through Particle Design. *Small* **2011**, *7*, 1919−1931.

(3) Nie, Z.; Petukhova, A.; Kumacheva, E. Properties and Emerging Applications of Self-Assembled Structures Made from Inorganic Nanoparticles. *Nat. Nanotechnol.* **2010**, *5*, 15−25.

(4) Lavik, E.; von Recum, H. The Role of Nanomaterials in Translational Medicine. *ACS Nano* **2011**, *5*, 3419−3424.

(5) Martín, R.; Menchón, C.; Apostolova, N.; Victor, V. M.; Alvaro, M.; Herance, J. R.; García, H. Nano-Jewels in Biology. Gold and Platinum on Diamond Nanoparticles as Antioxidant Systems Against Cellular Oxidative Stress. *ACS Nano* **2010**, *4*, 6957−6965.

(6) Chan, K. Y.; Ding, J.; Ren, J.; Cheng, S.; Tsang, K. Y. Supported Mixed Metal Nanoparticles as Electrocatalysts in Low Temperature Fuel Cells. *J. Mater. Chem.* **2004**, *14*, 505−516.

(7) Jain, P. K.; Huang, X.; El-Sayed, I. H.; El-Sayed, M. A. Noble Metals on the Nanoscale: Optical and Photothermal Properties and Some Applications in Imaging, Sensing, Biology, and Medicine. *Acc. Chem. Res.* **2008**, *41*, 1578−1586.

(8) Petros, R. A.; DeSimone, J. M. Strategies in the Design of Nanoparticles for Therapeutic Applications. *Nat. Rev. Drug Discovery* **2010**, *9*, 615−627.

(9) Martín, R.; Alvaro, M.; Herance, J. R.; García, H. Fenton-Treated Functionalized Diamond Nanoparticles as Gene Delivery System. *ACS Nano* **2010**, *4* (1), 65−74.

(10) Rojas, S.; Gispert, J. D.; Martín, R.; Abad, S.; Menchón, C.; Pareto, D.; Víctor, V. M.; Alvaro, M.; García, H.; Herance, J. R. Biodistribution of Amino-Functionalized Diamond Nanoparticles. In Vivo Studies Based on ^{18}F Radionuclide Emission. *ACS Nano* **2011**, *5*, 5552−5559.

(11) Devaraj, N. K.; Keliher, E. J.; Thurber, G. M.; Nahrendorf, M.; Weissleder, R. ^{18}F Labeled Nanoparticles for In Vivo PET-CT Imaging. *Bioconjugate Chem.* **2009**, *20*, 397−401.

(12) Guerrero, S.; Herance, J. R.; Rojas, S.; Mena, J. F.; Gispert, J. D.; Acosta, G. A.; Albericio, F.; Kogan, J. M. Synthesis and In Vivo Evaluation of the Biodistribution of a ^{18}F-Labeled Conjugate Gold-Nanoparticle-Peptide with Potential Biomedical Application. *Bioconjugate Chem.* **2012**, *23*, 399−408.

(13) Chrastina, A.; Schnitzer, J. E. Iodine-125 Radiolabeling of Silver Nanoparticles for In Vivo SPECT Imaging. *Int. J. Nanomed.* **2010**, *5*, 653−659.

(14) Schluep, T.; Hwang, J.; Hildebrandt, I. J.; Czernin, J.; Choi, C. H.; Alabi, C. A.; Mack, B. C.; Davis, M. E. Pharmacokinetics and Tumor Dynamics of the Nanoparticle IT-101 from PET Imaging and Tumor Histological Measurements. *Proc. Natl. Acad. Sci. U.S.A.* **2009**, *106*, 11394−11399.

(15) Pressly, E. D.; Rossin, R.; Hagooly, A.; Fukukawa, K.; Messmore, B. W.; Welch, M. J.; Wooley, K. L.; Lamm, M. S.; Hule, R. A.; Pochan, D. J.; Hawker, C. J. Structural Effects on the Biodistribution and Positron Emission Tomography (PET) Imaging of Well-Defined (64)Cu-Labeled Nanoparticles Comprised of Amphiphilic Block Graft Copolymers. *Biomacromolecules* **2007**, *8*, 3126−3134.

(16) Zhang, Y.; Sun, Y.; Xu, X.; Zhang, X.; Zhu, H.; Huang, L.; Qi, Y.; Shen, Y. M. Synthesis, Biodistribution, and Microsingle Photon Emission Computed Tomography (SPECT) Imaging Study of Technetium-99m Labeled PEGylated Dendrimer Poly(amidoamine) (PAMAM)-Folic Acid Conjugates. *J. Med. Chem.* **2010**, *53*, 3262−3272.

(17) Turner, S.; Lazar, S.; Freitag, B.; Egoavil, R.; Verbeeck, J.; Put, S.; Strauven, Y.; Van Tendeloo, G. High Resolution Mapping of Surface Reduction in Ceria Nanoparticles. *Nanoscale* **2011**, *3*, 3385−3390.

(18) Esch, F.; Fabris, S.; Zhou, L.; Montini, T.; Africh, C.; Fornasiero, P.; Comelli, G.; Rosei, R. Electron Localization Determines Defect Formation on Ceria Substrates. *Science* **2005**, *309*, 752−755.

(19) Deshpande, S.; Patil, S.; Kuchibhatla, S. V. N. T.; Seal, S. Size Dependency Variation in Lattice Parameter and Valency States in Nanocrystalline Cerium Oxide. *Appl. Phys. Lett.* **2005**, *87*, 133113/1−133113/3.

(20) Patil, S.; Seal, S.; Guo, Y.; Schulte, A.; Norwood, J. Role of Trivalent La and Nd Dopants in Lattice Distortion and Oxygen Vacancy Generation in Cerium Oxide Nanoparticles. *Appl. Phys. Lett.* **2006**, *88*, 243110/1−243110/3.

(21) Chiang, Y. M.; Lavik, E. B.; Blom, D. A. Defect Thermodynamics and Electrical Properties of Nanocrystalline Oxides: Pure and Doped CeO_2. *Nanostruct. Mater.* **1998**, *9*, 633−642.

(22) Chikyow, T.; Ahmet, P.; Nakajima, K.; Koida, T.; Takakura, M.; Yoshimoto, M.; Koinuma, H. A Combinatorial Approach in Oxide/Semiconductor Interface Research for Future Electronic Devices. *Appl. Surf. Sci.* **2001**, *189*, 284−291.

(23) Kamada, K.; Moriyasu, A. Photo-Excited Electroless Deposition of Semiconducting Oxide Thin Films and Their Electrocatalytic Properties. *J. Mater. Chem.* **2011**, *21*, 4301−4306.

(24) Dutta, G.; Saha, S. K.; Waghmare, U. V. Effects of Zr and Ti Doping on the Dielectric Response of CeO_2: A Comparative First-Principles Study. *Solid State Commun.* **2010**, *150*, 2020−2022.

(25) Wu, Z.; Li, M.; Overbury, S. H. On the Structure Dependence of CO Oxidation Over CeO_2 Nanocrystals with Well-Defined Surface Planes. *J. Catal.* **2011**, *285*, 61−73.

(26) Gaudillère, C.; Vernoux, P.; Mirodatos, C.; Caboche, G.; Farrusseng, D. Screening of Ceria-Based Catalysts for Internal Methane Reforming in Low Temperature SOFC. *Catal. Today* **2010**, *157*, 263−269.
(27) Chueh, W. C.; Haile, S. M. Ceria as a Thermochemical Reaction Medium for Selectively Generating Syngas or Methane from H_2O and CO_2. *ChemSusChem* **2009**, *2*, 735−739.
(28) de Lima, S. M.; Colman, R. C.; Jacobs, G.; Davis, B. H.; Souza, K. R.; de Lima, A. F. F.; Appel, L. G.; Mattos, L. V.; Noronha, F. B. Hydrogen Production from Ethanol for PEM Fuel Cells. An Integrated Fuel Processor Comprising Ethanol Steam Reforming and Preferential Oxidation of CO. *Catal. Today* **2009**, *146*, 110−123.
(29) Yao, H. C.; Yao, Y. F. Y. Ceria in Automotive Exhaust Catalysts: I. Oxygen Storage. *J. Catal.* **1984**, *86*, 254−265.
(30) Duprez, D.; Descorme, C.; Birchem, T.; Rohart, E. Oxygen Storage and Mobility on Model Three-Way Catalysts. *Top. Catal.* **2001**, *16*−*17*, 49−56.
(31) Maupin, I.; Mijoin, J.; Barbier, J., Jr.; Bion, N.; Belin, T.; Magnoux, P. Improved Oxygen Storage Capacity on CeO_2/Zeolite Hybrid Catalysts. Application to VOCs Catalytic Combustion. *Catal. Today* **2011**, *176*, 103−109.
(32) Navalon, S.; de Miguel, M.; Martin, R.; Alvaro, M.; Garcia, H. Enhancement of the Catalytic Activity of Supported Gold Nanoparticles for the Fenton Reaction by Light. *J. Am. Chem. Soc.* **2011**, *133*, 2218−2226.
(33) Hegde, M. S.; Madras, G.; Patil, K. C. Noble Metal Ionic Catalysts. *Acc. Chem. Res.* **2009**, *42*, 704−712.
(34) Binet, C.; Daturi, M.; Lavalley, J. C. IR Study of Polycrystalline Ceria Properties in Oxidised and Reduced States. *Catal. Today* **1999**, *50*, 207−225.
(35) Trovarelli, A. *Catalysis by Ceria and Related Materials*; Catalytic Sicence Series; Imperial College Press: London, 2002; Vol. 2; pp 85−168.
(36) Vivier, L.; Duprez, D. Ceria-Based Solid Catalysts for Organic Chemistry. *ChemSusChem* **2010**, *3*, 654−678.
(37) Dasa, M.; Patilb, S.; Bhargavaa, N.; Kanga, J.-F.; Riedela, L. M.; Sealb, S.; Hickmana, J. J. Auto-Catalytic Ceria Nanoparticles Offer Neuroprotection to Adult Rat Spinal Cord Neurons. *Biomaterials* **2007**, *28* (10), 1918−1925.
(38) Karakoti, A. S.; Monteiro-Riviere, N. A.; Aggarwal, R.; Davis, J. P.; Narayan, R. J.; Self, W. T.; McGinnis, J.; Seal, S. Nanoceria as Antioxidant: Synthesis and Biomedical Applications. *JOM* **2008**, *60* (3), 33−37.
(39) Heckert, E. G.; Karakoti, A. S.; Seal., S.; Self, W. T. The Role of Cerium Redox State in the SOD Mimetic Activity of Nanoceria. *Biomaterials* **2008**, *29* (18), 2705−2709.
(40) Colon, J.; Herrera, L.; Smith, J.; Patil, S.; Komanski, C.; Kupelian, P.; Seal, S.; Jenkins, D. W.; Baker, C. H. Protection from Radiation-Induced Pneumonitis Using Cerium Oxide Nanoparticles. *J. Nanomed. Nanotechnol.* **2009**, *5* (2), 225−231.
(41) Karakoti, A. S.; Singh, S.; Kumar, A.; Malinska, M.; Kuchibhatla, S. V. N. T.; Wozniak, K.; Self, W. T.; Seal, S. PEGylated Nanoceria as Radical Scavenger with Tunable Redox Chemistry. *J. Am. Chem. Soc.* **2009**, *131* (40), 14144−14145.
(42) Hirst, S. M.; Karakoti, A. S.; Tyler, R. D.; Sriranganathan, N.; Seal, S.; Reilly, C. M. Anti-inflammatory Properties of Cerium Oxide Nanoparticles. *Small* **2009**, *5* (24), 2848−2856.
(43) Estevez, A. Y.; Pritchard, S.; Harper, K.; Aston, J. W.; Lynch, A.; Lucky, J. J.; Ludington, J. S.; Chatani, P.; Mosenthal, W. P.; Leiter, J. C.; Andreescu, S.; Erlichman, J. S. Neuroprotective Mechanisms of Cerium Oxide Nanoparticles in a Mouse Hippocampal Brain Slice Model of Ischemia. *Free. Radical Biol. Med.* **2011**, *51*, 1155−1163.
(44) Korsvik, C.; Patil, S.; Seal, S.; Self, W. T. Superoxide Dismutase Mimetic Properties Exhibited by Vacancy Engineered Ceria Nanoparticles. *Chem. Commun.* **2007**, *14*, 1056−1058.
(45) Tarnuzzer, R. W.; Colon, J.; Patil, S.; Seal, S. Vacancy Engineered Ceria Nanostructures for Protection from Radiation-Induced Cellular Damage. *Nano Lett.* **2005**, *5*, 2573−2577.
(46) Niu, J.; Azfer, A.; Rogers, L. M.; Wang, X.; Kolattukudy, P. E. Cardioprotective Effects of Cerium Oxide Nanoparticles in a Transgenic Murine Model of Cardiomyopathy. *Cardiovasc. Res.* **2007**, *73*, 549−559.
(47) Gojova, A.; Lee, J. T.; Jung, H. S.; Guo, B.; Barakat, A. I.; Kennedy, I. M. Effect of Cerium Oxide Nanoparticles on Inflammation in Vascular Endothelial Cells. *Inhalation Toxicol.* **2009**, *21*, 123−130.
(48) He, X.; Zhang, H.; Ma, Y.; Bai, W.; Zhang, Z.; Lu, K.; Ding, Y.; Zhao, Y.; Chai, Z. Lung Deposition and Extrapulmonary Translocation of Nano-Ceria After Intratracheal Instillation. *Nanotechnology* **2010**, *21*, 285103.
(49) Geraets, L.; Oomen, A. G.; Schroeter, J. D.; Coleman, V. A.; Cassee, F. R. Tissue Distribution of Inhaled Micro- and Nano-Sized Cerium Oxide Particles in Rats: Results from a 28-Day Exposure Study. *Toxicol. Sci.* **2012**, *127* (2), 463−473.
(50) Park, E.-J.; Park, Y.-K.; Park, K. Acute Toxicity and Tissue Distribution of Cerium Oxide Nanoparticles by a Single Oral Administration in Rats. *Toxicol. Res.* **2009**, *25* (2), 79−84.
(51) Hardas, S. S.; Butterfield, D. A.; Sultana, R.; Tseng, M. T.; Dan, M.; Florence, R. L.; Unrine, J. M.; Graham, U. M.; Wu, P.; Grulke, E. A.; Yokel, R. A. Brain Distribution and Toxicological Evaluation of a Systemically Delivered Engineered Nanoscale Ceria. *Toxicol. Sci.* **2010**, *116*, 562−576.
(52) Dan, M.; Wu, P.; Grulke, E. A.; Graham, U. M.; Unrine, J. M.; Yokel, R. A. Ceria-Engineered Nanomaterial Distribution in, and Clearance from, Blood: Size Matters. *Nanomedicine (London)* **2012**, *7*, 95−110.
(53) Dan, M.; Tseng, M. T.; Wu, P.; Unrine, J. M.; Grulke, E. A.; Yokel, R. A. Brain Microvascular Endothelial Cell Association and Distribution of a 5 nm Ceria Engineered Nanomaterial. *Int. J. Nanomed.* **2012**, *7*, 4023−4036.
(54) Yokel, R. A.; Florence, R. L.; Unrine, J. M.; Tseng, M. T.; Graham, U. M.; Wu, P.; Grulke, E. A.; Sultana, R.; Hardas, S. S.; Butterfield, D. A. Biodistribution and Oxidative Stress Effects of a Systemically-Introduced Commercial Ceria Engineered Nanomaterial. *Nanotoxicology* **2009**, *3* (3), 234−248.
(55) Yokel, R. A.; Au, T. C.; Macphail, R.; Hardas, S. S.; Butterfield, D. A.; Sultana, R.; Goodman, M.; Tseng, M. T.; Dan, M.; Haghnazar, H.; Unrine, J. M.; Graham, U. M.; Wu, P.; Grulke, E. A. Distribution, Elimination and Biopersistence to 90 Days of a Systemically-Introduced 30 nm Ceria Engineered Nanomaterial in Rats. *Toxicol. Sci.* **2012**, *127*, 256−268.
(56) Hirst, S. M.; Karakoti, A.; Singh, S.; Self, W.; Tyler, R.; Seal, S.; Reilly, C. M. Bio-Distribution and In Vivo Antioxidant Effects of Cerium Oxide Nanoparticles in Mice. *Environ Toxicol.* doi:10.1002/tox.20704
(57) Abad, A.; Corma, A.; Garcia, H. Catalyst Parameters Determining Activity and Selectivity of Supported Gold Nanoparticles for the Aerobic Oxidation of Alcohols: The Molecular Reaction Mechanism. *Chem.—Eur. J.* **2008**, *14*, 212−222.
(58) Mäding, P.; Füchtner, F.; Wüst, F. Module-Assisted Synthesis of the Bifunctional Labelling Agent *N*-Succinimidyl 4-[^{18}F]-Fluorobenzoate ([18F]SFB). *Appl. Radiat. Isot.* **2005**, *63*, 329−332.
(59) Zhang, Z.; Yu, L.; Liu, W.; Song, Z. Surface Modification of Ceria Nanoparticles and their Chemical Mechanical Polishing Behavior on Glass Substrate. *Appl. Surf. Sci.* **2010**, *256*, 3856−3861.
(60) Corma, A.; Garcia, H. Silica-Bound Homogenous Catalysts as Recoverable and Reusable Catalysts in Organic Synthesis. *Adv. Synth. Catal.* **2006**, *384*, 391−1412.
(61) Silverstein, R. M.; Bassler, G. C.; Morrill, T. C. *Spectroscopic Identification of Organic Compounds*, 4th ed.; John Wiley: New York, 1981.